

Thermal effects on Common Rail injection system hydraulic performance

*Original*

Thermal effects on Common Rail injection system hydraulic performance / Ferrari, A., Vento, O.. - In: INTERNATIONAL JOURNAL OF ENGINE RESEARCH. - ISSN 1468-0874. - 24:8(2023), pp. 3602-3612. [10.1177/14680874231162412]

*Availability:*

This version is available at: 11583/2977423 since: 2023-05-31T09:02:44Z

*Publisher:*

SAGE

*Published*

DOI:10.1177/14680874231162412

*Terms of use:*

This article is made available under terms and conditions as specified in the corresponding bibliographic description in the repository

*Publisher copyright*

Sage postprint/Author's Accepted Manuscript

Ferrari, Alessandro; Vento, Oscar, Thermal effects on Common Rail injection system hydraulic performance, accepted for publication in INTERNATIONAL JOURNAL OF ENGINE RESEARCH (24 8) pp. 3602-3612. © 2023 (Copyright Holder). DOI:10.1177/14680874231162412

(Article begins on next page)

# 1 Thermal effects on Common Rail injection system hydraulic 2 performance

3 **Alessandro Ferrari, Oscar Vento<sup>(\*)</sup>**

4 *Energy Department, Politecnico di Torino, corso Duca degli Abruzzi 24, 10129, Torino, Italy*

6 *(\*) Corresponding author. Email: oscar.vento@polito.it*

## 7 **1. Abstract**

8 The effect of the fuel temperature on the hydraulic performance of a Common Rail diesel injector has  
9 been investigated with an integrated experimental-numerical approach. An experimental campaign  
10 pertaining to single and double injections has been performed for fuel tank temperatures ranging from  
11 28°C to 68°C. In general, an augment in the injected mass has been observed for increasing values of the  
12 fuel tank temperature. Moreover, the interaction between the main and after injection changes with the  
13 temperature and the dwell time threshold for fusion-free injections increases with the fuel temperature.  
14 The temperature at the injector nozzle has been measured and compared with that obtained with a thermo-  
15 fluid dynamics simple model, showing that the real temperature and the estimated one correlate well.  
16 The influence of the fuel temperature on the internal injector dynamic has been explored by means of a  
17 validated 1D numerical model of the injector thermo-fluid dynamics. The main direct effect of the  
18 temperature variation concerns the needle lift, which reaches a larger peak value for a higher fuel  
19 temperature: this explains the general increment in the injected mass and the augmented value of the  
20 injection fusion threshold for the main-after injections. The obtained results could allow more accurate  
21 open-loop control strategies for the injected mass, which include thermal effects, to be implemented.

## 22 **2. Introduction**

23 The fuel injection apparatus has a key role in a powertrain, since engine efficiency [1], combustion [2]  
24 and pollutant emissions [3] are significantly influenced by the injection schedule and for this reason the  
25 injection system further development continues to be a research challenge even for alternative fuels.

26 The Common Rail (CR) fuel injection apparatus offers great flexibility in terms of number of injection  
27 events per engine cycle, dwell-times between shots and high injection pressure (up to 3000 bar) [4]. The  
28 designed shape and quantity of every fuel shot affect combustion and engine-out emission control [5]

29 and both design parameters, associated to the injector structure [6], and physical factors, such as the fuel  
30 properties [7] or the ambient conditions [8], must be taken into account. Fractioning the injection quantity  
31 between multiple shots with close-to-zero hydraulic dwell-times according to digital rate shaping  
32 strategies, can allow combustion noise to be reduced significantly [9]. An ultra-high injection pressure  
33 coupled with small injection holes allow optimal level of fuel atomization, mixture homogeneity and  
34 easy evaporation [10]. Soot and hydrocarbon (*HC*) emission reduction can be obtained, thanks to the  
35 diminished liquid length and the consequent reduced impingement on walls, and it can be coupled with  
36 a  $\text{NO}_x$  decrease if high EGR rates are simultaneously applied [11]. Besides, an optimal number of orifices  
37 and an ideal angular position of them in the nozzle are able to affect the inter- and near-nozzle flow  
38 patterns, thus positively affecting lift-off flame and jet interaction with the squish regions [12].

39 By investigating the influence of low temperature (for both the fuel and the injector body) it has been  
40 seen that an injector equipped with a pressure balanced valve shows a pronounced reduction of the fuel  
41 injected quantity under cold conditions (the reference temperature was 40 °C for the fuel and 90 °C for  
42 the injector body) while a three-way valve injector features negligible differences in the injected mass at  
43 800 bar of rail pressure and a progressive increment of the fuel quantity delivered beyond this rail  
44 pressure level [13].

45 The effect of the injected fuel temperature has been analysed with reference to the spray development  
46 and the combustion evolution. For both diesel fuel and DME (dimethyl ether), the higher is the fuel  
47 temperature, the earlier is the evaporation and the lower the fuel plume penetration. This causes a lower  
48 maximum combustion pressure and a more delayed start of combustion: both these effects lead to a  
49 reduction in the  $\text{NO}_x$  emissions [14, 15]. Furthermore, a reduction in the fuel temperature can cause a  
50 higher non-uniformity degree in the fuel-air mixture, which can increase the time necessary to reach a  
51 constant level of evaporation rate and can lead to augmented emissions in unburned *HC* [16]. A  
52 significant sensitivity of fuel economy and  $\text{NO}_x$  emission level to the fuel temperature at the injector  
53 nozzle has been noticed even for a biodiesel fuelled engine, especially if low EGR rate is used [17].

54 When a pure biodiesel (B100), characterized by a high viscosity, is considered, the injected fuel  
55 temperature can become crucial to improve the biodiesel spray performance. In fact, an increase in the  
56 fuel temperature enlarges the spray angle cone and the spray area, which are usually smaller at a fixed  
57 temperature if compared with normal diesel fuel. Furthermore, even the pump efficiency improves, due  
58 to the reduced viscous friction losses, since fuel viscosity reduces with fuel temperature [18].

59 The flow through the injection system circuit is not isothermal. The major source of heat input to the fuel  
60 in the tank during system working is the fuel recirculated from the injectors [19]. The fuel in the tank  
61 reaches the injector inlet after the pumping phase, which determines a temperature increment of about 1  
62 °C every 100 bar of compression [20]. Concerning the temperature evolution within the injector, it has  
63 been often predicted in the literature with an isothermal flow assumption [21, 22]. However, with this  
64 hypothesis, the temperature rise, due to the viscous dissipation through the injector restrictions and due  
65 to the pressure drop, is not simulated [23]. The variations in density, viscosity [21] and bulk modulus  
66 [24] with temperature can affect the injector behaviour. In a ballistic injector, where the needle never  
67 reaches the upper stroke-end under the usual operating conditions [25], the needle dynamics significantly  
68 depends on the pressure and viscous forces which are affected by the temperature [26]. As far as the  
69 nozzle holes are concerned, a complex temperature pattern can be identified with 3D numerical  
70 simulation, and a separated behaviour between the boundary layer and the core flow is often highlighted.  
71 If a 2000 bar injection is considered, the maximum temperature difference in the flow can reach 80 °C  
72 between the fluid at the core region and the one at the walls, which is a remarkable value if the  
73 temperature dependence of the fuel properties is taken into account [27]. All this highlights a significant  
74 role of thermal aspects in the hydraulic performance with effects on the spray.  
75 In the present work, temperature effects on the injector working are analysed. With regard to the  
76 hydraulic performance, the temperature at the injector nozzle hole exit has been measured and compared  
77 with the one obtained by means of a simple thermodynamic model. Furthermore, a 1D numerical model  
78 has been employed to investigate the injector internal dynamics dependence on the fuel temperature.  
79 Numerical and experimental tests on single and double injections have been considered in a wide range  
80 of nominal rail pressures under different values of the fuel temperature in the tank.

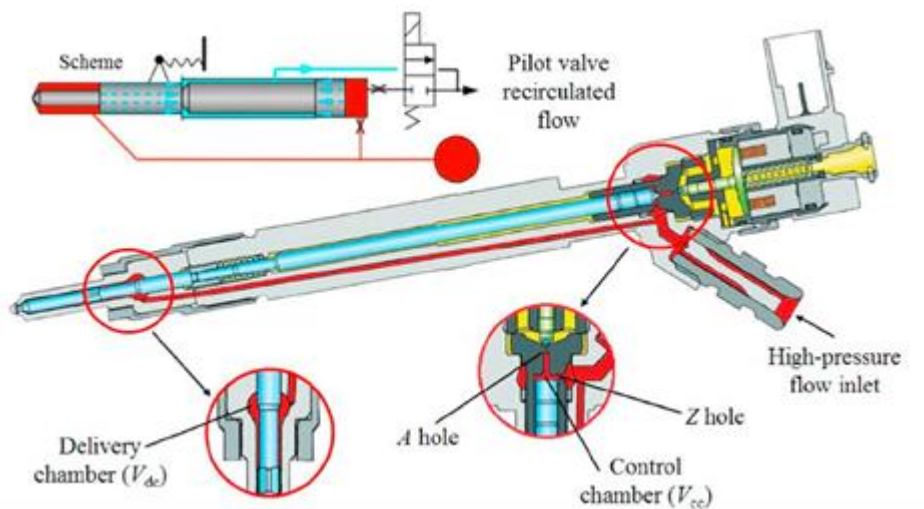
### 81 **3. Experimental facility**

82 Experimental tests were performed in the Internal Combustion Engines Laboratory at the Politecnico di  
83 Torino by means of the Moehwald-Bosch hydraulic test bench for fuel injection systems (maximum  
84 speed: 6100 rpm, maximum torque: 100 Nm, nominal power: 35 kW).

85 The selected calibration fluid is the Shell V-Oil 1404 (ISO 4113) since it is capable to satisfactorily  
86 reproduce diesel oil properties up to 150 °C over the entire pressure range.

87 Tests were conducted on a Bosch CR injection system for a 4 cylinders passenger car diesel engine. A  
88 high-pressure rotary pump, featuring a displacement of 430 mm<sup>3</sup>/rev and a double effect single piston, is

89 employed to feed the rail. The rail is connected with solenoid-actuated CRI 2.18 injectors, a scheme of  
90 which is reported in Fig. 1. The high-pressure fuel enters the injector and a part of it reaches the delivery  
91 chamber (volume  $V_{dc}$ ) upstream the nozzle zone, and the other part, through the Z hole, fills the control  
92 chamber (volume  $V_{cc}$ ). As soon as the electrical current supplied by the Electronic Control Unit (ECU)  
93 is switched on, the injector solenoid is energized and the control chamber discharges fuel from the pilot  
94 valve through the A hole. Therefore, the pressure forces acting on the needle become unbalanced and the  
95 latter moves up, opening the nozzle and allowing the fuel injection. When the ECU switches off the  
96 current to the solenoid, the closure of the pilot valve makes the pressure rise in the control chamber,  
97 therefore the needle starts its closure phase, which finishes when its tip touches the seat. Hence, the  
98 nozzle is again closed and injection ends [9]. The injected fuel quantity depends on both the time-  
99 averaged value of the injection pressure and on the hydraulic duration of the injection, which is related  
100 to the electrical command to the solenoid, i.e. the energizing time ( $ET$ ) [28].



101

102

103

**Figure 1. CRI 2.18 injector.**

104 A piezoresistive transducer has been mounted at the injector inlet along the rail-to-injector pipe to  
105 measure the pressure time history ( $p_{inj,in}$ ) and this datum will be used as a boundary condition for the  
106 numerical model. The transducer measuring range is up to 2000 bar and its linearity error is lower than  
107  $\pm 0.1\%$  of the fuel scale value. It has been assumed that the only uncertainty contribution that affects the  
108 transducer accuracy is the linearity error, which is lower than  $\pm 2$  bar.

109 The injected flow-rate and the injected mass have been measured by means of the HDA flowmeter. In  
110 this instrument the pressure in a closed volume is measured, together with the speed of sound (for which

111 an ultrasonic sensor is employed), then, by following Zeuch's method, the injected mass flow-rate is  
112 obtained [29].

113 The fuel temperature at the nozzle hole exit has been measured by means of a PT100 temperature sensor  
114 mounted at a distance of 25 mm from the injector tip along a duct with a counterpressure of 40 bar where  
115 the fuel is injected. The same injector previously mounted in the HDA to detect the injected flow-rate  
116 has then been made inject the fuel in the pipe with the PT100 sensor to measure the fuel temperature  
117 under the same controlled working conditions.

118 Single injections, together with pilot-main and main-after injections, have been considered in this  
119 research investigation. Tests have been performed by varying the  $ET$  at different nominal rail pressure  
120 ( $p_{nom}$ ) values for single injections, while for double injections the  $ET$  values for the considered injections  
121 have been kept constant and the dwell time between the shots has been varied. The fuel temperature at  
122 the pump inlet was varied from 28 °C to 68 °C. In particular, 28°C represents the minimum value that  
123 can be controlled by the current test bench, 40 °C is usually assumed as the reference temperature for  
124 hydraulic tests by the fuel injection system manufacturers and 68 °C represents the maximum  
125 temperature that can be reached on the test bench for safety reasons. The hydraulic test bench can heat  
126 the fuel in the tank by means of a heating coil and, at the pump inlet, the fuel temperature is controlled  
127 by means of a heat exchanger where the cooling water flowrate is regulated in order to fulfil the fuel  
128 temperature requirement (the fuel temperature at the pump inlet is measured by means of a temperature  
129 probe that represents the feedback signal to modify the cooling water flowrate). Tests have been  
130 performed at a pump speed of 2000 rpm.

#### 131 **4. Fuel properties and temperature in the injection apparatus**

132 The temperature can affect the fuel properties significantly. The ones here considered are the density ( $\rho$ ),  
133 the bulk modulus ( $E$ ), the dynamic viscosity ( $\mu$ ) and the thermal expansivity ( $\beta$ ), which is defined as  
134  $-\frac{1}{\rho} \left( \frac{\partial \rho}{\partial T} \right)_p$ . Figure 2 reports the trends of the ISO 4113 oil properties, experimentally determined, as  
135 functions of the temperature for different nominal rail pressures, according to [21]: symbols stand for the  
136 experimental values, whereas the solid lines correspond to the determined polynomial interpolating  
137 expressions.

138 The test rig can control the tank oil temperature ( $T_{tank}$ ). By assuming an isentropic evolution of the fuel  
139 through the pump compression, the temperature increase, due to the pressure rise, can be estimated.

140 If the fundamental thermodynamic state relation [30] is considered for an isentropic compression, one  
 141 has:

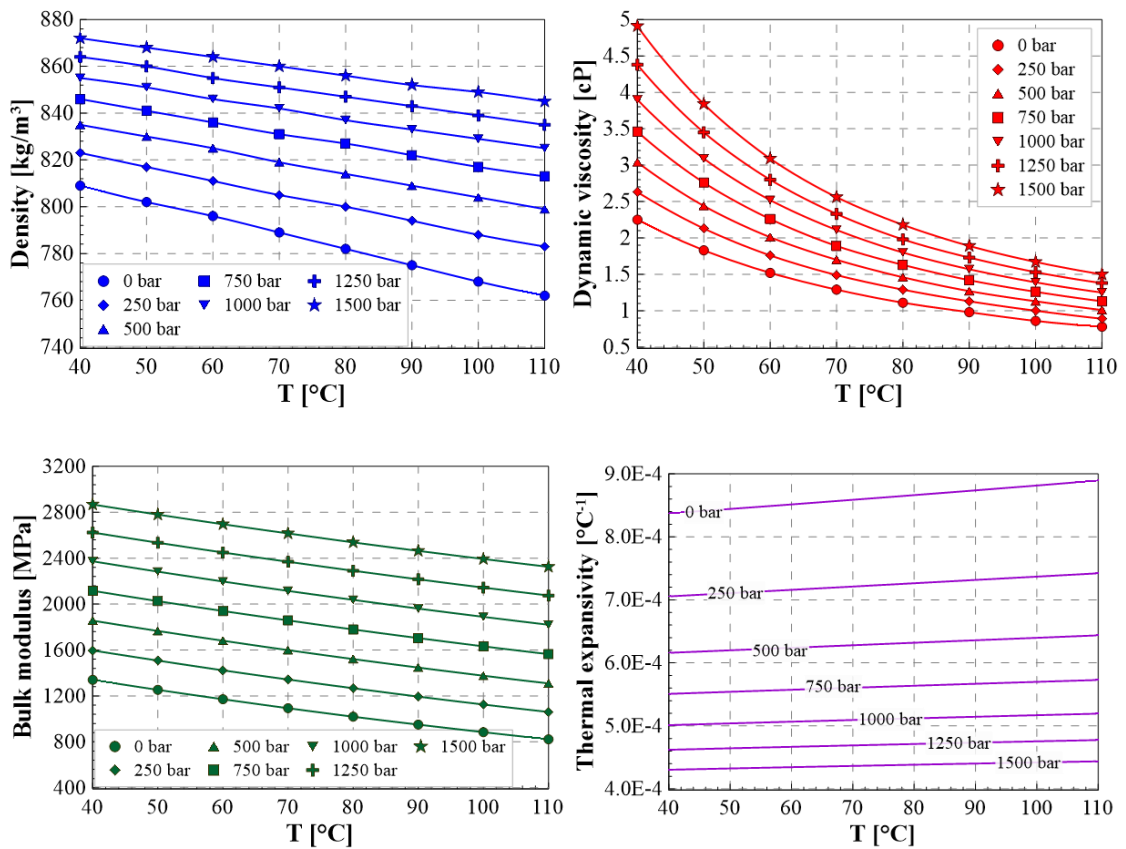
$$142 \quad dh = \frac{dp}{\rho} \quad (1)$$

143 where  $h$  is the enthalpy per unit of mass. For a liquid, the enthalpy is defined as:

$$144 \quad dh = c_p dT + (1 - \beta T) \frac{dp}{\rho} \quad (2)$$

145 where  $c_p$  is the specific heat at constant pressure. By combining Eqs. (1) and (2), one obtains:

$$146 \quad c_p dT = \beta T \frac{dp}{\rho} \quad (3)$$



147

148 **Figure 2. ISO 4113 oil properties with respect temperature and pressure.**

149

150 Hence an estimation of the temperature level in the high-pressure circuit can be obtained for a certain  
 151 nominal rail pressure.

152 The fuel temperature through the injector can be estimated by considering an isenthalpic evolution [21],

153 if the injector is roughly regarded as a set of localized restrictors. The injected fuel temperature can

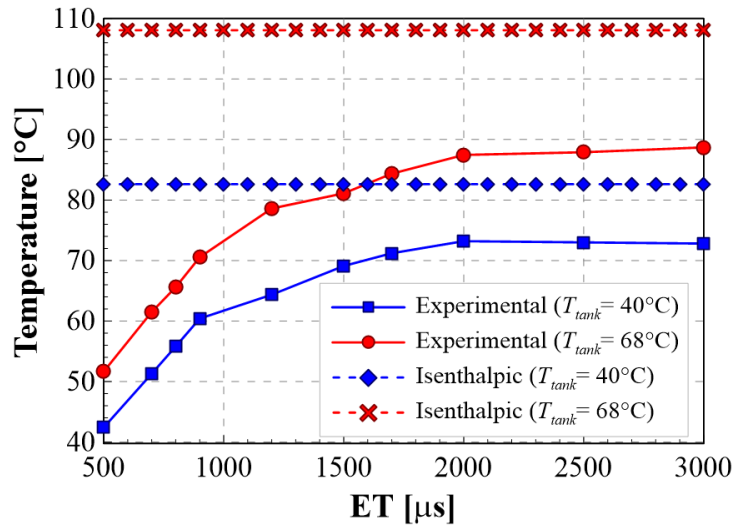
154 therefore be predicted as follows:

$$155 \quad c_p dT = (\beta T - 1) \frac{dp}{\rho} \quad (4)$$

## 156 **5. Experimental results**

157 Figure 3 reports the trend of the fuel temperature measured at the nozzle hole exit with respect to  $ET$ ;  
158 data refers to  $p_{nom}=800$  bar and to both  $T_{tank}=40$  °C and  $T_{tank}=68$  °C. Tests were also performed at  $T_{tank}=$   
159  $28$ °C and measure fuel temperatures resulted slightly lower than the corresponding ones at  
160  $T_{tank}=40$  °C. After a certain value of  $ET$ , the measured temperature reaches an asymptotic value. This  
161 can be interpreted by considering the measuring procedure used to obtain the temperature value. When  
162  $ET$  is small, the injected flow-rate is not high enough to let the sensor measure a steady-state temperature  
163 in the pipe where the fuel is injected. Therefore, if the  $ET$  is increased, the detected temperature augments  
164 and finally reaches an asymptotic value, which is the steady-state one that should be considered in the  
165 comparison with the isenthalpic model. The asymptotic values measured for different nominal rail  
166 pressures (cf. Fig. 3) have been adopted as the fuel temperatures at the nozzle outlet in the numerical  
167 simulations.

168 In Fig. 4, the measured oil temperature at the nozzle exit for  $ET=3000$   $\mu$ s is plotted (with symbols) with  
169 respect to the correspondent isenthalpic temperature obtained for a certain rail pressure under the  
170 adiabatic assumption, for both  $T_{tank}=40$  °C and  $T_{tank}=68$  °C. Although the curves are well distinct from  
171 the bisector and the isenthalpic assumption overestimates the real temperature (the injector is less  
172 dissipative than a restrictor) the estimations provided can be reasonable. Furthermore, the experimental  
173 and isenthalpic temperatures are well correlated, and the correlation is almost linear (cf. the continuous  
174 lines in Fig. 4). Hence, for a fixed  $T_{tank}$  and a given rail pressure level, the isenthalpic temperature at the  
175 nozzle can be obtained by means of Eq. (4) and a more accurate estimation of the real temperature can  
176 be obtained by means of a correlation curve which can be determined for each injector typology.

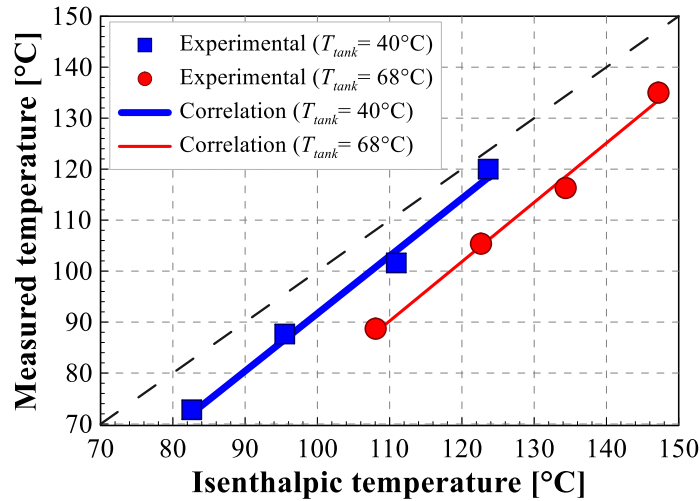


177

178

179

Figure 3. Fuel temperature at the injector exit for different ET and  $T_{tank}$  values ( $p_{nom} = 800$  bar).



180

181

182

183

Figure 4. Correlation between the measured temperature at the injector outlet and the isenthalpic temperature.

184 Tests for single injections have been performed over a wide range of nominal rail pressure (between 600

185 bar and 1800 bar) and of  $ET$  (between 350  $\mu s$  and 1000  $\mu s$ ) in order to explore the entire range of working

186 conditions for a diesel passenger car. Figure 5 shows the injector characteristics pertaining to different

187 nominal rail pressure levels and to two distinct fuel tank temperatures, namely 40 °C and

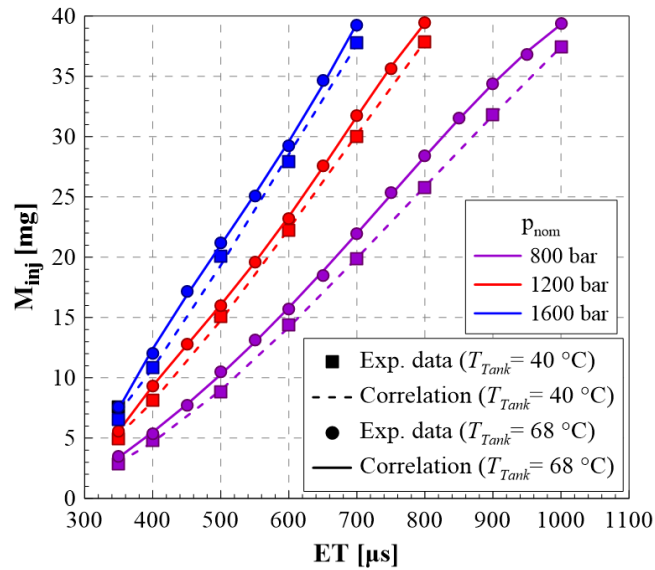
188 68 °C. As can be inferred from Fig. 5, the injected mass generally increases with the fuel temperature for

189 a fixed working condition in terms of  $p_{nom}$  and  $ET$ .

190 Figure 6 reports the injected flow-rates for  $p_{nom}=1600$  bar and  $ET= 600 \mu s$ , at two different  $T_{tank}$  values.

191 It can be observed that the injection temporal length ( $ITL$ ) increases with the tank fuel temperature, and

192 this leads to an augmented injected fuel quantity for fixed  $ET$  and  $p_{nom}$ . [31].

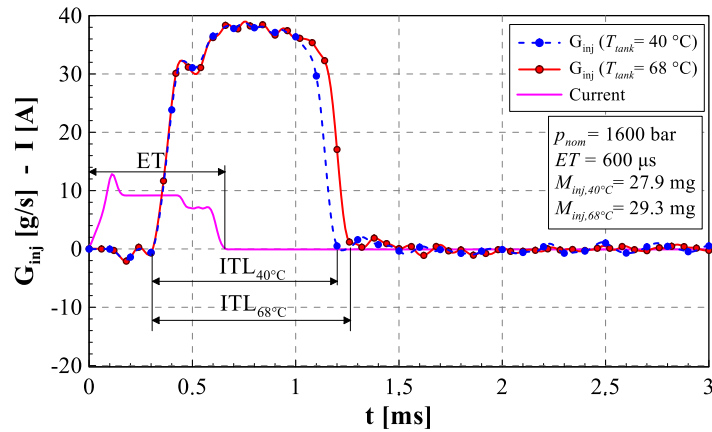


193

194

195

Figure 5. Injector characteristics for different nominal rail pressure levels and fuel tank temperatures.



196

197

198

Figure 6. Injected flow-rate for different fuel tank temperature values ( $p_{nom} = 1600$  bar,  $ET = 600$   $\mu s$ ).

199

200

201

202

203

204

205

206

207

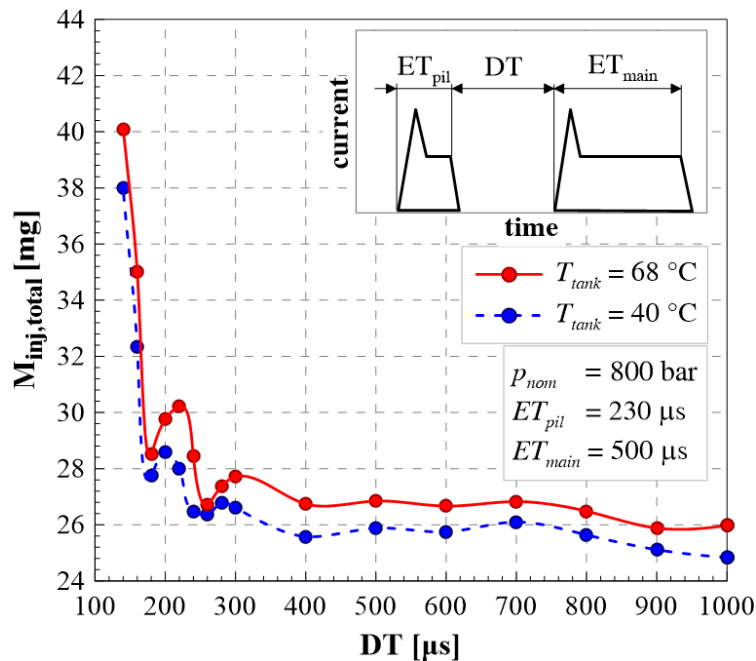
208

As far as the double injections experimental campaign is concerned, a CRI 2.20 injector has been employed. This injector, differently from the CRI 2.18 used for the analysis on single injections, features a Minirail in place of the delivery chamber (the latter corresponds to volume  $V_{dc}$  in Fig. 1) in order to reduce the injected mass fluctuation of the second shot with respect to the dwell time [25]. It has been already verified that also the CRI 2.20 injector is affected by a thermal drift similar that of the CRI 2.18 injector, and an augment in the injected mass can be detected as the fuel temperature increases [31]. Pertaining to pilot-main injections, a  $DT$  sweep has been reported in Fig. 7, referring to  $p_{nom} = 800$  bar,  $ET_{pil} = 230$   $\mu s$  and  $ET_{main} = 500$   $\mu s$ . The overall injected mass  $M_{inj,total}$  (given by the sum of pilot and main injected masses), measured by means of the HDA, has been reported at different  $DT$  values for both  $T_{tank} = 40^\circ C$  (blue curve) and  $T_{tank} = 68^\circ C$  (red curve). The injected mass increases with the temperature, as

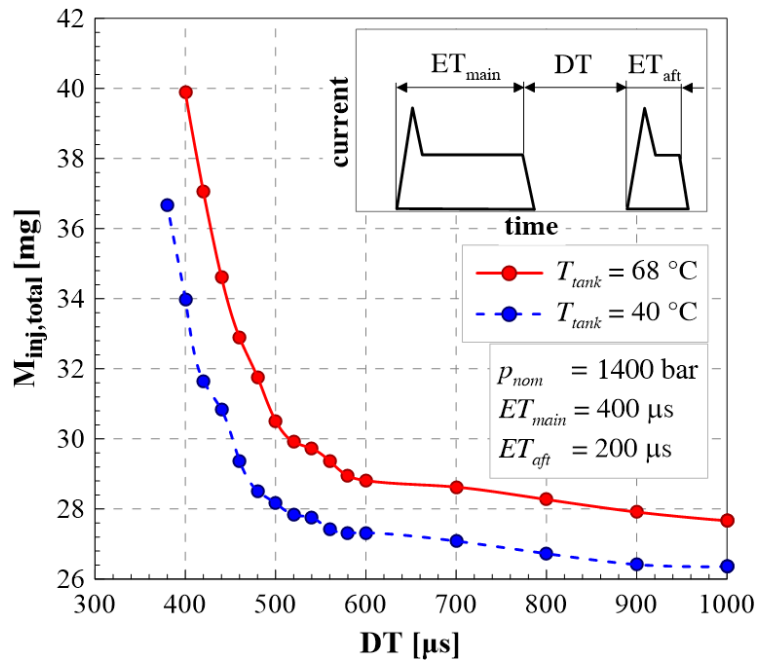
209 occurs for single injections, while the dynamic features of the system, such as the injection fusion  
 210 threshold, do not vary appreciably.

211 Regarding main-after injections, the overall injected mass with respect to the dwell time value is  
 212 represented in Figure 8 for the case  $p_{nom} = 1400$  bar,  $ET_{main} = 400$   $\mu$ s,  $ET_{aft} = 200$   $\mu$ s at two different fuel  
 213 tank temperatures, i.e.  $T_{tank} = 40^\circ$ C (blue curve) and  $T_{tank} = 68^\circ$ C (red curve). The most evident effect is,  
 214 even in this case, an augment in the injected mass when the fuel temperature increases. Moreover, it can  
 215 be observed that the injection fusion threshold, that is the minimum dwell-time value for which two  
 216 injections are still hydraulically distinct, increases with the temperature. This is obvious in Figure 9,  
 217 where the injected flowrates for the  $DT = 540$   $\mu$ s case is reported for both  $T_{tank} = 40^\circ$ C (blue curve, the  
 218 main and after injection are still separated), and  $T_{tank} = 68^\circ$ C, (red curve, where the needle never closes  
 219 the nozzle holes during the entire injection event).

220 Many strategies can be implemented on the ECU to correct the injection schedules in order to compensate  
 221 for the abovementioned fuel temperature effects. As an example, the main energizing time can be  
 222 modified according to the engine water cooling temperature, by means of an open-loop strategy,  
 223 through an empirical coefficient. The presented thermo-fluid dynamic model allows the temperature of  
 224 the injected fuel, which considers the temperature increase due to both the fuel compression in the high-  
 225 pressure pump and the fuel expansion across the injector, to be used to refine the open-loop control  
 226 strategy of the injected mass.



227  
 228 **Figure 7. Pilot-main injection  $DT$  sweep for different fuel tank temperatures.**  
 229

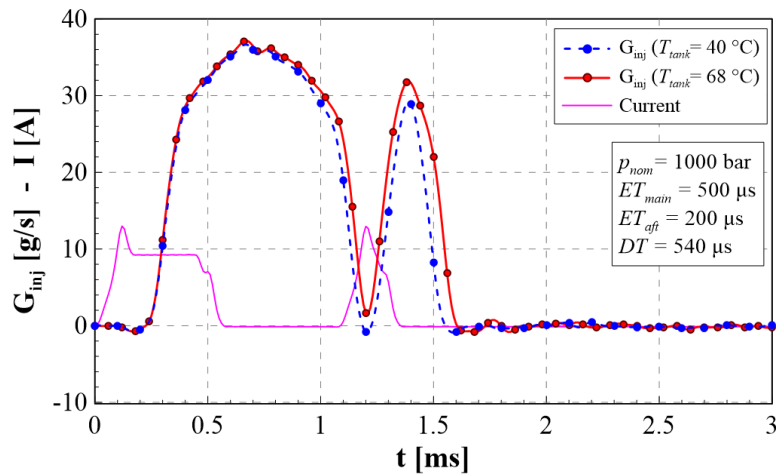


230

231

232

Figure 8. Main-after injection  $DT$  sweep for different fuel tank temperatures.



233

234

235

Figure 9. Injected flow-rate for a main-after injection for different fuel tank temperatures.

236

## 6. Model description

237

238

239

240

241

242

243

The analysis regarding single injection is based on a 1D injector numerical diagnostic tool developed in [32, 33] and further validated at different fuel temperatures. A scheme of the 1D model is represented in Fig. 10. The circuit generally consists of a network of 0D chambers connected by means of 1D pipes [34]. The boundary conditions consist of the measured pressure time history at the injector inlet along the rail-to-injector pipe and of the electrical current signal provided to the solenoid of the pilot valve. By selecting these boundary conditions, any inaccuracy, due to the modelling of the rail, the injector feeding pipe, the pump and the ECU, can be avoided.

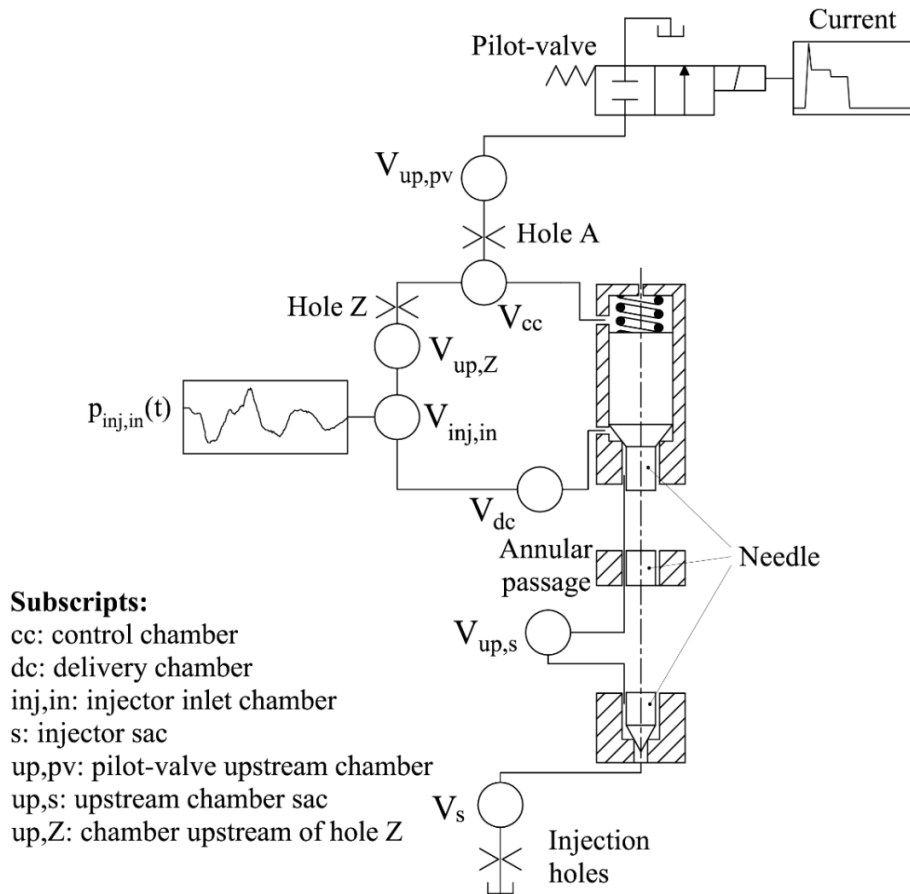
244 During the needle movement, a viscous force is generated between the needle and the injector body, due  
 245 to the presence of a thin boundary layer. The flow in the small annular passage (cf. Fig. 10) is laminar  
 246 and follows Poiseuille's law. The viscous friction force in this zone can therefore be evaluated as [35]:

$$247 \quad F_{fric} = \frac{\mu L_c v \pi \cdot d_n}{\delta_r} \quad (5)$$

248 where  $d_n$  is the needle diameter,  $L_c$  represents the length of the annular passage,  $\delta_r$  is the radial distance  
 249 between the needle and the injector holder and  $v$  is the velocity of the needle.

250 The needle movement is related to the pressure variation in the control chamber, that is to the control  
 251 chamber discharge and refilling through the A and Z holes, respectively (cf. Fig. 10). The Z hole is in a  
 252 non-cavitating condition, whereas the A hole can experience cavitation conditions [36]. One important  
 253 point in thermal models concerns the discharge coefficient of the holes.

254



255

256 **Figure 10. Scheme of the 1D numerical model.**

257

258 The discharge coefficient of a hole is defined as the ratio of the effective flow-rate to the ideal one,  
 259 obtained by means of the Bernoulli equation for a liquid flow [37].

260 For a cavitation-free hole the discharge coefficient  $C_d$  has been defined as follows [38]:

$$261 \quad C_d = C_{d,max} \cdot \tanh\left(\frac{2 \cdot Re}{Re_{crit}}\right) \quad (6)$$

262 where  $C_{d,max}$  is the maximum value of the discharge coefficient,  $Re$  is the Reynolds number and  $Re_{crit}$   
263 is the critical Reynolds number, where the transition between laminar and turbulent flow occurs. The  
264 Reynolds number is calculated in the following way:

$$265 \quad Re = \frac{D}{\mu} \cdot \sqrt{2\Delta p\rho} \quad (7)$$

266 where  $D$  is the hole diameter and  $\Delta p$  the pressure drop across the hole.

267 When the flow through the hole can be subjected to cavitation phenomena, the cavitation number  $CN$  can  
268 be introduced [39]:

$$269 \quad CN = \frac{p_{in} - p_v}{p_{in} - p_{out}} \quad (8)$$

270 where  $p_{in}$ ,  $p_{out}$  and  $p_v$  are the pressure value at the inlet of the hole, at the outlet of the hole and the  
271 vapour pressure of the fuel, respectively. When  $CN$  is lower than a critical cavitation number ( $CN_{crit}$ )  
272 which is experimentally obtained, cavitation occurs, and the discharge coefficient is calculated by  
273 considering the actual cavitation number  $CN$  and the contraction coefficient  $C_c$  according to this  
274 expression [40]:

$$275 \quad C_d = C_c \cdot \sqrt{CN} \quad (9)$$

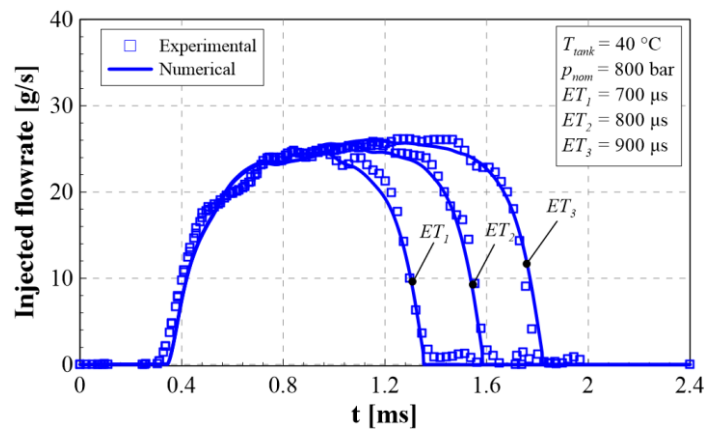
276 In the present investigation, the flow coefficient pertaining to Z hole was evaluated with Eqs. (6) and  
277 (7), whereas the complete model of  $C_d$  which includes Eqs. (6-9) was implemented for A hole and for  
278 the injection holes in order to simulate possible cavitation occurrences.

## 279 **6.1 Numerical model results**

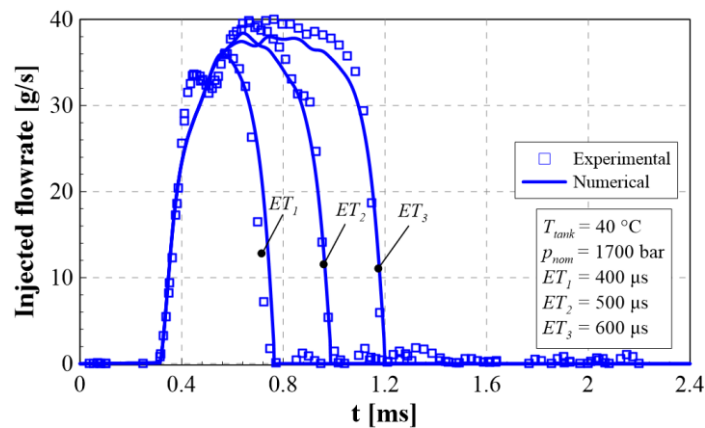
280 Figure 11 shows the comparison between the experimental injected flow-rates (plotted with symbols)  
281 and the numerical ones (plotted with continuous line) for the two pressure levels 800 bar (Fig. 11a), and  
282 1700 bar (Fig. 11b). The  $T_{tank}$  was set at 40°C and the results pertaining to different  $ET$ s have been  
283 reported in the plots. The corresponding results referring to  $T_{tank} = 68$  °C have been plotted in Fig. 12. It  
284 can be observed that the numerical results match the experimental ones accurately.

285 In Fig. 13, the numerical control chamber pressure traces have been reported for both  $T_{tank} = 40$  °C and  
286  $T_{tank} = 68$  °C ( $p_{nom} = 800$  bar and  $ET = 800$  μs). As can be inferred, the difference in fuel temperature does  
287 not affect significantly the pressure time history in the control chamber because both the flow-rates

288 through the Z and A holes are almost the same for the two cases. This is in line with the results available  
 289 in the literature, where the effect of the fuel temperature on the control chamber pressure and flow-rates  
 290 through A and Z holes are significant only when the fuel temperature within the injector is below 0° C  
 291 [36]. From the numerical model it results that the A hole is experiencing cavitating condition for both  
 292 the tested  $T_{tank}$  temperatures and only a small increase in the  $CN$  can be noticed for  $T_{tank} = 40^{\circ}\text{C}$ , leading  
 293 to a slight augment in the  $C_d$  value. Instead, the Z hole doesn't undergo any cavitating regime and the  
 294 flow is turbulent for both  $T_{tank} = 40^{\circ}\text{C}$  and  $T_{tank} = 68^{\circ}\text{C}$ .  
 295 Figure 14 reports the numerical pressure time histories detected in the delivery chamber ( $p_{dc}$ ), in the  
 296 upstream-sac chamber ( $p_{up,s}$ ) and in the injector sac ( $p_{sac}$ ) (cf. Fig. 10 for the chambers location), as well  
 297



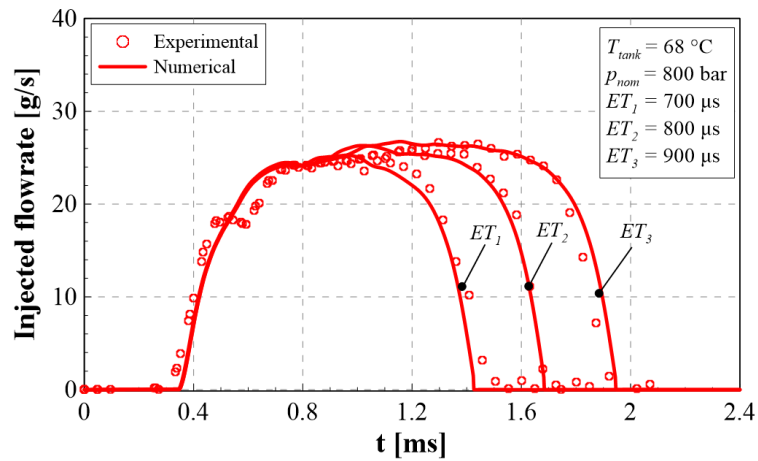
(a)



(b)

301 **Figure 11. Experimental injected flow-rates compared with the numerical ones with  $T_{tank} = 40^{\circ}\text{C}$ ,**  
 302  **$p_{nom} = 800$  bar (a),  $p_{nom} = 1700$  bar (b).**  
 303 as the needle lift numerical trace ( $p_{nom}=800$  bar,  $ET=1000$  us,  $T_{tank}=40^{\circ}\text{C}$ ). The temperature at the injector  
 304 inlet (cf.  $V_{inj,in}$  in Fig. 10) is provided as an input datum to the injector model and has been obtained by  
 305 means of Eq. (3). For the other injector chambers, starting from the injector inlet temperature, the  
 306

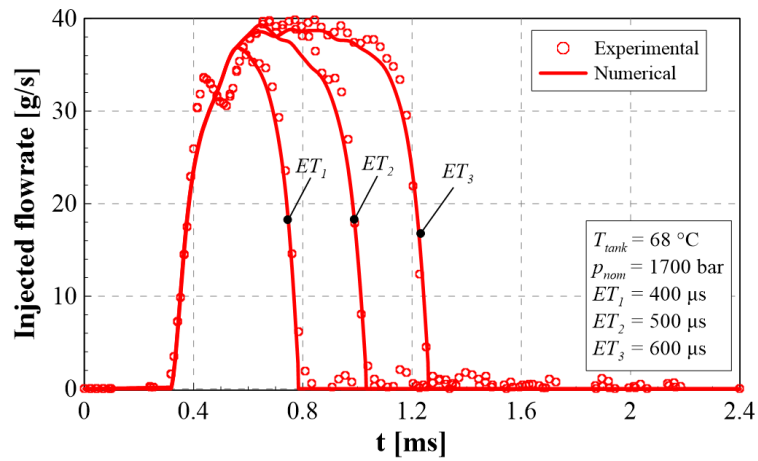
307 instantaneous pressure difference between two adjacent chambers (cf.  $\Delta p_{dc \rightarrow up,s}$ ,  $\Delta p_{up,s \rightarrow sac}$  and  $\Delta p_{sac \rightarrow cyl}$   
 308 in Fig. 14) is used to estimate the temperature rise under the  $h=const$  hypothesis  
 309 and, by means of the correlation reported in Fig. 4, an estimation of the real temperature can be obtained.  
 310 If the isenthalpic temperature results to be outside from the considered range in Fig. 4, a linear  
 311 extrapolation has been performed. In fact, based on data of fuel temperature measured at the nozzle exit  
 312 for a wide range of  $p_{nom}$  values in [41], it was possible to extend the linear correlations reported in Fig. 4  
 313 up to about 160 °C (for  $T_{tank}=40$  °C) and to about 180 °C (for  $T_{tank}=68$  °C).



314

315

(a)



316

317

(b)

318 **Figure 12. Experimental injected flow-rates compared with the numerical ones with  $T_{tank} = 68$  °C,**  
 319  **$p_{nom} = 800$  bar (a),  $p_{nom} = 1700$  bar (b).**

320

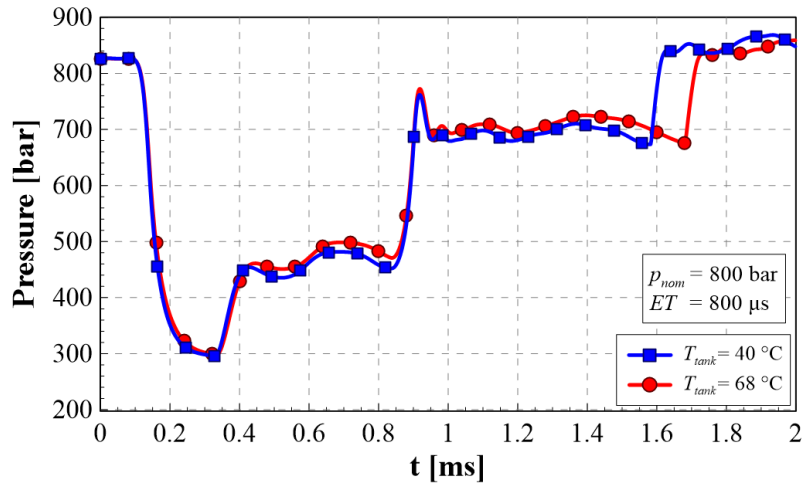


Figure 13. Pressure in the control chamber for  $T_{tank} = 40\text{ °C}$  and  $68\text{ °C}$ ,  $p_{nom} = 800\text{ bar}$ ,  $ET = 800\text{ μs}$ .

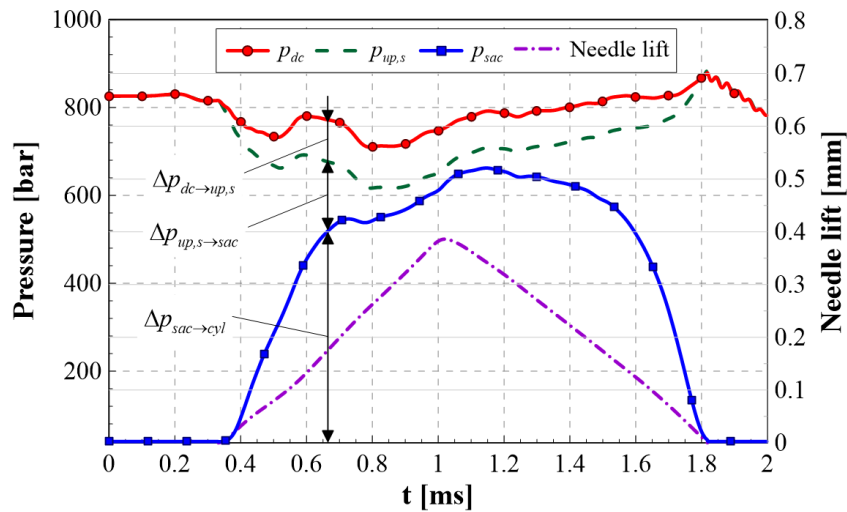
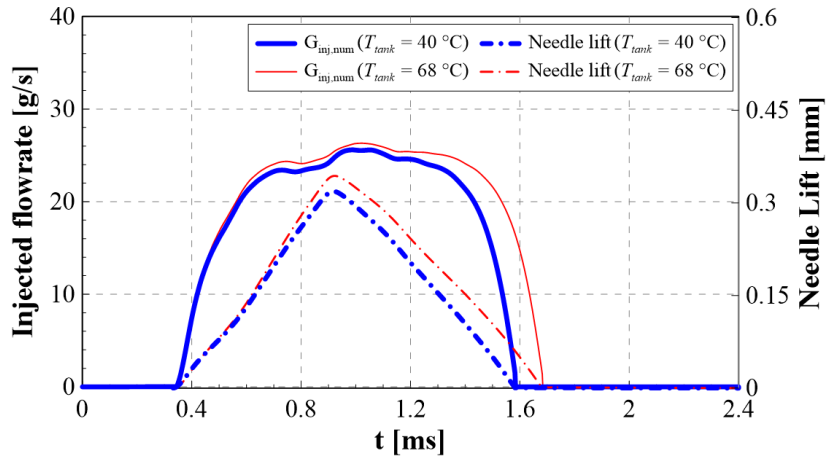


Figure 14. Pressure time histories and needle lift from the numerical model,  $p_{nom} = 800\text{ bar}$ ,  $ET = 800\text{ μs}$ ,  $T_{tank} = 40\text{ °C}$ .

321  
322  
323  
324

325  
326  
327  
328

329 At the beginning and at the end of the injection event, the pressure drop  $\Delta p_{up,s \rightarrow sac}$  is larger than  $\Delta p_{sac \rightarrow cyl}$   
330 (cf. Fig. 14) because the restricted flow area is at the needle-seat passage. Therefore, the fuel heating  
331 phase mainly occurs when the fuel flows across the passage between the needle and its seat. On the other  
332 hand, when the needle lift is sufficiently high and the flow-rate is controlled by the nozzle holes,  $\Delta p_{sac \rightarrow cyl}$   
333 becomes much larger than  $\Delta p_{up,s \rightarrow sac}$ , hence the fuel heating mainly occurs through the nozzle holes.  
334 In Fig. 15 the numerical needle lift time distribution is reported, for both the considered  $T_{tank}$   
335 temperatures, together with the numerical injected flow-rates ( $p_{nom} = 800\text{ bar}$ ,  $ET = 800\text{ μs}$ ). Figure 16  
336 plots the same quantities as in Fig. 15 but with reference to a different working condition ( $p_{nom} = 1700$   
337 bar,  $ET = 600\text{ μs}$ ).



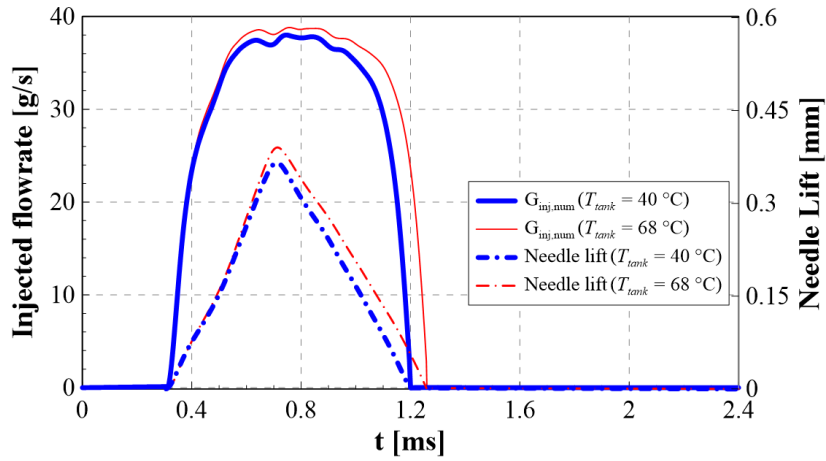
338

339

340

341

Figure 15. Injected flowrate and needle lift for  $T_{tank} = 40\text{ }^{\circ}\text{C}$  and  $68\text{ }^{\circ}\text{C}$ ,  $p_{nom} = 800\text{ bar}$ ,  $ET = 800\text{ }\mu\text{s}$ .



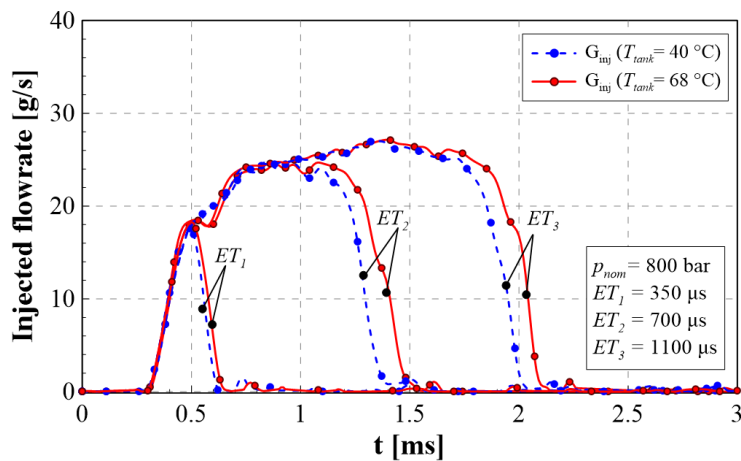
342

343

344

345

Figure 16. Injected flowrate and needle lift for  $T_{tank} = 40\text{ }^{\circ}\text{C}$  and  $68\text{ }^{\circ}\text{C}$ ,  $p_{nom} = 1700\text{ bar}$ ,  $ET = 600\text{ }\mu\text{s}$ .



346

347

348

349

Figure 17. Injected flow-rates for different  $ET$  values with  $T_{tank} = 40\text{ }^{\circ}\text{C}$  and  $68\text{ }^{\circ}\text{C}$ ,  $p_{nom} = 800\text{ bar}$ . In general, since the fuel viscosity reduces with the temperature (the decreasing trend is exponential in Fig. 2), the viscous force acting on the needle diminishes as the fuel temperature augments. Therefore,

350 due to the reduced viscous force, the needle velocity increases during the opening phase as  $T_{tank}$  augments,  
351 leading to a higher needle peak lift value under a fixed  $ET$ . Then, after the electrical current is switched  
352 off, the needle starts its closure phase and, the higher is the temperature, the larger is the needle  
353 downstroke required to close the nozzle, and therefore the longer are the nozzle closure delay and the  
354 injection duration.

355 The effect of the fuel temperature is less obvious for injections characterized by small  $ET$ s, as is shown  
356 in Fig. 17. In fact, a shorter- $ET$  injection is characterized by a smaller needle lift peak value and the  
357 absolute variation of the latter with  $T_{tank}$  is small. Hence, the higher is the needle lift peak value, the more  
358 evident is the effect of the fuel temperature in the final part of the injected flow-rate.

359 In [36] it has been verified that, even for a CRI 2.20 injector, the main effect of the fuel temperature, in  
360 the considered range, is given by a reduced viscous force acting on the needle, which leads to a higher  
361 needle lift peak. Therefore, for the pilot-main injections, the higher needle lift peak obtained at higher  
362 fuel temperature leads to a general increment in the mass, although the injection fusion threshold does  
363 not change considerably, as shown in Fig. 7. Instead, for main-after injections, when the tank fuel  
364 temperature grows, an augment in the injection fusion threshold can be detected, together with an  
365 increment in the injected mass (cf. Figs. 8-9). The injection fusion threshold increment is justified, since  
366 the tendency to reach higher needle-lift peak values for larger fuel temperatures becomes more evident  
367 for longer injections (cf. Fig 17): unlike pilot-main schedules, the shot with the larger  $ET$  is the former  
368 in main-after injections.

369

## 370 **7. Conclusions**

371 The fuel temperature effect on the hydraulic performance of a CR injection system has been analyzed by  
372 means of both experimental and numerical results. The major findings can be summarized as follows:

- 373 - the experimental campaign on single and double injections (pilot-main and main-after schedules) has  
374 shown that, when the fuel temperature increases, the injected mass generally grows. Furthermore, the  
375 fuel temperature appreciably affects the injection fusion threshold of the main-after injections;
- 376 - the injected fuel temperature has been measured along a pipe where the fuel is injected, at a distance of  
377 25 mm from the injector tip. This experimental temperature has been compared successfully with the one  
378 obtained by means of a newly developed simple thermo-fluid dynamics model: starting from the fuel  
379 tank temperature, and by considering an isentropic compression through the pump, the fuel temperature

380 at the injector entrance has been obtained. Furthermore, by means of an isenthalpic evolution assumption  
381 across the injector, the final temperature at the nozzle exit has been calculated;  
382 - a 1D numerical model has been used to investigate the injector dynamics at different fuel temperatures.  
383 The most relevant effect of the fuel temperature increase is the reduction in the fuel viscosity, which  
384 leads to a diminished viscous force that acts against the needle movement. When the fuel temperature  
385 increases, the needle reaches an augmented peak value, which explains the experimental differences with  
386 respect to the fuel temperature for both single and double injections;  
387 - the 1D numerical model shows that the fuel heating inside the injector occurs primarily in  
388 correspondence of the needle seat passage, with an effect on the beginning and end of the injection law,  
389 as well as across the nozzle holes with an effect on the central part of the injection law;  
390 - an innovative open-loop control strategy of the injected mass, based on the estimated nozzle exit fuel  
391 temperature, could be designed to improve the compensation of the injector thermal drifts during engine  
392 operation (the current strategies are usually based on the water cooling temperature).

## 393 **8. References**

- 394 [1] Beatrice, C., Di Blasio, G., Pesce, F.C., Vassallo, A. et al., “Key Fuel Injection System Features for  
395 Efficiency Improvement in Future Diesel Passenger Cars,” *SAE Int. J. Advances & Curr. Prac. in*  
396 *Mobility* 1(3):1084-1099, 2019.
- 397 [2] Yang F, Yao C, Wang J, Ouyang M. “Load expansion of a dieseline compression ignition engine  
398 with multi-mode combustion”. *Fuel* 2016;171:5-17.
- 399 [3] Vakiti, K., Deussen, J., Pilger, C., Nanjundaswamy, H., Szailer, T., Franke, M., Tomazic, D., Thomas,  
400 K., Romijn, M., Deppenkemper, K., and Vagnoni, G. “In-Use Compliance Opportunity for Diesel  
401 Powertrains,” SAE Technical Paper 2018-01-0877, 2018.
- 402 [4] Boccardo, G., F. Millo, A. Piano, L. Arnone, S. Manelli, Simon Fagg, P. Gatti, Olaf E. Herrmann,  
403 Dirk Queck and Jost Weber. “Experimental investigation on a 3000 bar fuel injection system for a SCR-  
404 free non-road diesel engine.” *Fuel* 243 (2019): 342-351.
- 405 [5] Niculae AL, Chiriac R, Racovitza A. Effects of Injection Rate Shape on Performance and Emissions  
406 of a Diesel Engine Fuelled by Diesel and Biodiesel B20. *Applied Sciences*. 2022; 12(3):1333.  
407 <https://doi.org/10.3390/app12031333>

408 [6] Kang, S., Lee, S., Hong, D., & Bae, C. (2022). Effects of Nozzle Orifice Diameter and Hole Number  
409 on Diesel Combustion and Engine Performance. *International Journal of Automotive Technology*, 23,  
410 481-494.

411 [7] Liu, H., Ma Jun-sheng, F. Dong, Y. Yang, X. Liu, Ma Gui-xiang, Z. Zheng and M. Yao.  
412 “Experimental investigation of the effects of diesel fuel properties on combustion and emissions on a  
413 multi-cylinder heavy-duty diesel engine.” *Energy Conversion and Management* 171 (2018): 1787-1800.

414 [8] Ma, Y., L. Cui, X. Ma and J. Wang. “Optical study on spray combustion characteristics of  
415 PODE/diesel blends in different ambient conditions.” *Fuel* 272 (2020): 117691.

416 [9] Ferrari, A., C. Novara, E. Paolucci, O. Vento, M. Violante and T. Zhang. “A new closed-loop control  
417 of the injected mass for a full exploitation of digital and continuous injection-rate shaping.” *Energy*  
418 *Conversion and Management* 177 (2018): 629-639.

419 [10] Zhai, C., Jin, Y., Wu, Q., Nishida, K., & Ogata, Y. (2021). Diesel spray and combustion of multi-  
420 hole injectors with micro-hole under ultra-high injection pressure – Combustion characteristics. *Fuel*,  
421 300, 120949.

422 [11] Wang, Xiangang, Zuohua Huang, W. Zhang, O. Kuti and K. Nishida. “Effects of ultra-high injection  
423 pressure and micro-hole nozzle on flame structure and soot formation of impinging diesel spray.” *Applied*  
424 *Energy* 88 (2011): 1620-1628.

425 [12] Moon, S., Y. Gao, S. H. Park, J. Wang, N. Kurimoto and Y. Nishijima. “Effect of the number and  
426 position of nozzle holes on in- and near-nozzle dynamic characteristics of diesel injection.” *Fuel* 150  
427 (2015): 112-122.

428 [13] Cavicchi, A., Postriotti, L., Pesce, F.C., and Ferrara, U., “Experimental Analysis of Fuel and  
429 Injector Body Temperature Effect on the Hydraulic Behavior of Latest Generation Common Rail  
430 Injection Systems,” SAE Technical Paper 2018-01-0282, 2018, doi:10.4271/2018-01-0282.

431 [14] Kubota, Masaru, K. Yoshida, H. Shoji and H. Tanaka. “8 A Study of the Influence of Fuel  
432 Temperature on Emission Characteristics and Engine Performance of Compression Ignition Engine.”  
433 SAE Technical Paper. (2002).

434 [15] Guangxin, Gao, Y. Zhu-lin, Zhou Apeng, Liu Sheng-hua and Wei Yanju. “Effects of Fuel  
435 Temperature on Injection Process and Combustion of Dimethyl Ether Engine.” *Journal of energy*  
436 *resources technology* 135 4 (2013): 422021-422025 .

- 437 [16] Babadi, M. N., S. Kheradmand and C. Bae. "Experimental and Computational Investigation of  
438 Diesel and Gasoline Injection in a Direct Injection Compression Ignition Engine." *International Journal*  
439 *of Automotive Technology* 21 (2020): 23-32.
- 440 [17] Mamat, R., Abdullah, N. R., Xu, H., Wyszynski, M. L., & Tsolakis, A. (2009). *Effect of fuel*  
441 *temperature on performance and emissions of a common rail diesel engine operating with rapeseed*  
442 *methyl ester (RME)* (No. 2009-01-1896). SAE Technical Paper.
- 443 [18] Anis, Samsudin and Galuh Nur Budiandono. "Investigation of the effects of preheating temperature  
444 of biodiesel-diesel fuel blends on spray characteristics and injection pump performances." *Renewable*  
445 *Energy* 140 (2019): 274-280.
- 446 [19] El-Sharkawy, A., "Transient Thermal Analysis of Diesel Fuel Systems," *SAE Int. J. Mater. Manf.*  
447 5(2):2012, doi:10.4271/2012-01-1049.
- 448 [20] A. Ferrari, Z. Jin, O. Vento, T. Zhang. An injected quantity estimation technique based on time-  
449 frequency analysis. *Control Eng Pract*, 116 (2021), 104910
- 450 [21] Catania, A., Ferrari, A., Manno, M., and Spessa, E., "Thermal Effect Simulation in High-Pressure  
451 Injection System Transient Flows," SAE Technical Paper 2004-01-0532, 2004.
- 452 [22] Payri, R., Salvador, F.J., Carreres, M., and Belmar-Gil, M., "An Investigation on the Fuel  
453 Temperature Variations Along a Solenoid Operated Common-Rail Ballistic Injector by Means of an  
454 Adiabatic 1D Model," SAE Technical Paper 2018-01-0275, 2018.
- 455 [23] Salvador, F., J. Gimeno, M. Carreres and M. Crialesi-Esposito. "Experimental assessment of the  
456 fuel heating and the validity of the assumption of adiabatic flow through the internal orifices of a diesel  
457 injector." *Fuel* 188 (2017): 442-451.
- 458 [24] Armas, O., S. Martínez-Martínez, C. Mata and C. Pacheco. "Alternative method for bulk modulus  
459 estimation of Diesel fuels." *Fuel* 167 (2016): 199-207.
- 460 [25] Ferrari, A. and Zhang T. "Influence of the injector setup on digital and continuous injection rate-  
461 shaping performance in diesel engine passenger cars." *Energy Conversion and Management* 205 (2020):  
462 112259.
- 463 [26] Kim, J., J. Lee and K. Kim. "Numerical study on the effects of fuel viscosity and density on the  
464 injection rate performance of a solenoid diesel injector based on AMESim." *Fuel* 256 (2019): 115912.

465 [27] Salvador, F., M. Carreres, J. D. L. Morena and E. Martínez-Miracle. "Computational assessment of  
466 temperature variations through calibrated orifices subjected to high pressure drops: Application to diesel  
467 injection nozzles." *Energy Conversion and Management* 171 (2018): 438-451.

468 [28] Ferrari, A., C. Novara, O. Vento, M. Violante and T. Zhang. "A novel fuel injected mass  
469 feedback-control for single and multiple injections in direct injection systems for CI engines" *Fuel*, 334  
470 (2023): 126670

471 [29] Postrioti, L., Giacomo Buitoni, F. Pesce and C. Ciaravino. "Zeuch method-based injection rate  
472 analysis of a common-rail system operated with advanced injection strategies." *Fuel* 128 (2014): 188-  
473 198.

474 [30] Bejan, Adrian. *Advanced engineering thermodynamics*. John Wiley & Sons, New York, 2016.

475 [31] Ferrari, A., C. Novara, E. Paolucci, O. Vento, M. Violante and T. Zhang. "Design and rapid  
476 prototyping of a closed-loop control strategy of the injected mass for the reduction of CO<sub>2</sub>, combustion  
477 noise and pollutant emissions in diesel engines." *Applied Energy* 232 (2018): 358-367.

478 [32] Ferrari, A. and O. Vento. "Influence of Frequency-Dependent Friction Modeling on the  
479 Simulation of Transient Flows in High-Pressure Flow Pipelines." *Journal of Fluids Engineering-*  
480 *transactions of The Asme* 142 (2020).

481 [33] Catania, A.E., Ferrari, A. and Manno, M., 2009, "Development and Application of a Complete  
482 Multijet Common-Rail Injection-System Mathematical Model for Hydrodynamic Analysis and  
483 Diagnostics", *ASME J Eng. Gas Turb. Power*, 130(6), pp. 062809-1:13.

484 [34] Jin, Z., Vento, O., Zhang, T., Ferrari, A., Mittica, A., Ouyang, L., and Tan, S. (March 4, 2021).  
485 "Numerical-Experimental Optimization of the Common-Feeding Injection System Concept for  
486 Application to Light-Duty Commercial Vehicles." *ASME. J. Energy Resour. Technol.* December 2021;  
487 143(12): 122304. <https://doi.org/10.1115/1.4050133>

488 [35] Blackburn JF, Reethof G, Shearer JL. "Fluid power control". MIT Press; 1960.

489 [36] Payri, R., F. Salvador, M. Carreres and J. D. L. Morena. "Fuel temperature influence on the  
490 performance of a last generation common-rail diesel ballistic injector. Part II: 1D model development,  
491 validation and analysis." *Energy Conversion and Management* 114 (2016): 376-391.

- 492 [37] Ferrari, A.. “Fluid dynamics of acoustic and hydrodynamic cavitation in hydraulic power  
493 systems.” *Proceedings of the Royal Society A: Mathematical, Physical and Engineering Sciences* 473  
494 (2017).
- 495 [38] McCloy, D. and H. Martin. "Control of Fluid Power : Analysis and design", 2<sup>nd</sup> edition. Ellis  
496 Horwood Limited 1980.
- 497 [39] Nurick WH. 1976, “Orifice cavitation and its effect on spray mixing.” *J. Fluids Eng.* 98, 681–689.
- 498 [40] Payri, R., J. M. García, F. Salvador and J. Gimeno. “Using spray momentum flux measurements to  
499 understand the influence of diesel nozzle geometry on spray characteristics.” *Fuel* 84 (2005): 551-561.
- 500 [41] Zhao, Jianhui, L. Grekhov and Peng-fei Yue. “Limit of Fuel Injection Rate in the Common Rail  
501 System under Ultra-High Pressures.” *International Journal of Automotive Technology* 21 (2020): 649-  
502 656.